Chloride diffusivity in hardened cement paste from microscale analyses and accounting for binding effects

P Carrara[1], L De Lorenzis[1] and D P Bentz[2]

[1] Technische Universität Braunschweig, Institute of Applied Mechanics, Bienroder Weg 87, 38106 Braunschweig, DE

[2] National Institute of Standards and Technology, Engineering Laboratory, Materials and Structural Systems Division, Stop 8615, 100 Bureau Drive, Gaithersburg, MD 20899-8615, USA

E-mail: p.carrara@tu-braunschweig.de, l.delorenzis@tu-braunschweig.de, dale.bentz@nist.gov

Abstract. The diffusion of chloride ions in hardened cement paste (HCP) under steady-state conditions and accounting for the highly heterogeneous nature of the material is investigated. The HCP microstructures are obtained through segmentation of X-ray images of real samples as well as from simulations using the cement hydration model CEMHYD3D. Moreover, the physical and chemical interactions between chloride ions and HCP phases (binding), along with their effects on the diffusive process, are explicitly taken into account. The homogenized diffusivity of the HCP is then derived through a least square homogenization technique. Comparisons between numerical results and experimental data from the literature are presented.

Keywords: Chloride diffusion and binding, Microscale analyses, Numerical analyses, Segmentation of real microstructures, Simulated microstructures

Submitted to: *Modelling Simul. Mater. Sci. Eng.*

1. Introduction

The diffusion of chlorides in reinforced concrete structures often controls their durability and its prediction is needed both to forecast service life and to schedule an efficient maintenance strategy [1–3]. Chloride ions can be found in hardened cement paste (HCP) either because they are present in the ingredients (water, cement clinker, supplementary cementitious materials, and/or aggregates), or as a consequence of diffusion from the external environment [4–6]. Other than using a chloride-based accelerator, the former case is mostly related to a modification of the production process of the cement clinker,

but is not likely to occur in typical practice since the presence of chlorides in concrete raw materials is generally restricted by production guidelines [4, 6]. Conversely, the penetration of chlorides from the external environment is of more practical interest since it is representative of many aggressive environments such as exposure to de-icing salts or marine/tidal environments [4].

The penetration of chlorides from the external environment is strongly influenced by the characteristics and the heterogeneous nature of the HCP at the microscopic level [7–9] (e.g., at a length scale of 1 μm and larger). In particular, the topological and physical characteristics of the capillary pore system [7, 10] and the possibility for the ions to have easy access to the pores are among the most important parameters governing the diffusion rate [7]. Also, the solid phases play a significant role for the chloride penetration into HCP, as the microporosity of the solid matrix constitutes a slower but effective pathway for ionic diffusion. Their effect becomes more important as the capillary porosity decreases, reaching a primary role in the HCP where the capillary pore system does not form a continuous (percolated) pathway in three dimensions [7]. Moreover, it is well known that some products of the hydration of the cement clinker can physically or chemically interact with chloride ions, modifying the diffusion processes through the so-called binding effect [1, 3, 4, 6, 11, 12].

The level of detail needed to study the diffusion at the microscopic level adds considerable complexity to experimental tests and their interpretation. For this reason, the problem is often addressed by computational modeling. The diffusion problem is classically addressed by adopting Ficks theory under some simplifying assumptions such as one-dimensional flow or the absence of binding (see [12–17] among others). More recently, Garboczi and Bentz [8] proposed a numerical model for diffusion based on the electrical conductivity-diffusivity analogy and discretization of the HCP using a 3-D lattice of conductors, each with a different diffusivity/conductivity as a function of the underlying phase. Based on such a model, an empirical relationship was developed to evaluate the diffusivity of the HCP at the mesoscale as a function of the capillary porosity. The same authors present in [1] a different model based on random walk theory applied to a discretized two-dimensional microstructure that also accounts for the interaction between chlorides and the solid phases. The electrical conductivity analogy and random walk approaches were subsequently combined [18] in a multiscale approach where the diffusivity of bulk cement paste and of the interfacial transition zone (ITZ) between the paste and the aggregates are defined at the microscale through the formula presented in [1], while accounting for the aggregate volume fraction at the mesoscale. Then, random walk theory similar to that proposed in [1] is used to simulate diffusion at the mesoscale, which is conceived as a three phase continuum medium composed of non-diffusive aggregates, bulk cement paste, and the ITZ. The model proposed in [18] is subsequently simplified through the introduction of analytical procedures [19].

A multiscale method is also adopted by Zhang et al. [9, 20], where the authors use Lattice-Boltzmann and finite element methods respectively for the micro- and mesoscales. Here, the authors use simulated microstructures and account also for the

diffusive behavior of the ITZ, however the binding effect is treated in a very simplified manner. Nilenius et al [21, 22] study the upscaling of the diffusive properties from the meso- to the macroscale, neglecting the microscale and thus the binding effect. The interaction between diffusion, binding, and the presence of cracks is investigated for a 3D structure broadly segmented into HCP and voids by Lu et al. in [23]. Finally, Ukrainczyk and Koenders in [10] investigate the mass transport at the microscale level and the role of the capillary pore system topology neglecting binding, while in [24] they employ a similar approach to study the transient phase of the calcium ion leaching process in HCP.

The main aim of the present work is to study the steady-state diffusion behavior of externally supplied chlorides in HCP accounting for its highly heterogeneous microstructure, as well as for physical and chemical binding effects acting at the single phase level (i.e., considering the various chemical compounds present). To this end, Ficks law of diffusion is modified through the consistent introduction of a phase-dependent binding activity coefficient. The 3D HCP microstructures for the analyses are both simulated, using CEMHYD3D [25, 26], as well as segmented starting from real X-ray computer tomography (CT) images available from the NIST Visible Cement Database [27, 28]. The model is implemented in a finite difference code and several tests are simulated varying the environmental chloride concentration. The diffusivity at the mesoscale is evaluated through a linear homogenization using both experimental data and widely accepted analytical relationships from the literature. A comparison between results from real and simulated HCP microstructures is also performed and discussed.

The paper is structured as follows: in section 2 the governing equations of diffusion coupled with binding are presented. In section 3 the effects of the binding are described and quantitatively evaluated. The numerical aspects of the implementation and the simulations performed are described respectively in section 4 and 5. Finally, some concluding remarks are made in section 6.

2. Chloride diffusion and binding

2.1. Governing equations for chloride diffusion in HCP

The migration of particles inside a medium should pointwise satisfy the general mass conservation condition, which reads

$$\frac{\partial C}{\partial t} = -\nabla \cdot \boldsymbol{J}\,, \tag{1}$$

where C is the particle concentration, t is the time and $\boldsymbol{J}$ is the flux vector.

To completely describe the motion of the particles, a flux constitutive relation is needed. When dealing with diffusion of ions in porous media, such as for the case of chloride diffusion in HCP studied here, the flux constitutive equation can be easily formulated taking into account the conditions in which the migration of ions takes place. Firstly, water saturated conditions are assumed since they are imposed in most

experimental setups and occur in many real-world cases due to the limited thickness of the concrete cover. Moreover, in absence of external forces inducing the motion of the fluid, advection can be neglected, leading to a pure diffusive process. It is also assumed here that the principal driving force responsible for the diffusion process is the ions concentration gradient, meaning that all other potential fields (e.g., electrical fields, presence of temperature or chemical potential gradients) are negligible.

With the above assumptions, the constitutive flux equation can be expressed through Fick's first law as

$$\boldsymbol{J} = -D\nabla C\,, \tag{2}$$

where D is the diffusion coefficient or diffusivity.

The definition of the diffusivity parameter D in Equation 2 is strongly related to the problem at hand. In particular, it is possible to distinguish between

- D^* or self-diffusion coefficient: it is defined as the diffusion coefficient of a species when the chemical potential gradient equals zero. It describes the mobility of a particle within other particles of the same species, i.e. it is a macroscopic description of the Brownian motion (bulk motion in homogeneous media);
- D_{free} or free diffusivity (also, inter-diffusivity): it describes the diffusivity of a binary system composed of the diffusive species and a solvent. It is related to the self-diffusion coefficient by the equation

$$D^* = D_{free}\frac{\partial \ln C_{diff}}{\partial \ln a_{diff}}\,, \tag{3}$$

  where C_{diff} and a_{diff} are the concentration and the chemical activity of the diffusive species. What is usually taken as a reference value is the diffusivity of a species into pure water at a constant temperature;
- D_c or diffusivity in saturated capillary pores: when migration takes place into small pores (i.e., diameter ≤ 5 μm to 10 μm), phenomena such as particle-environment interaction and the viscosity of the fluid become non negligible, thus reducing the diffusivity with respect to D_{free};
- D_s or solid diffusivity: diffusivity can take place also in those solid materials where the inner structural arrangement (e.g., clusters of crystal grains) involves the presence of micro- or nano-capillaries whose geometry cannot be resolved explicitly. In such cases, the value of diffusivity is defined by decreasing the value of D_c to account for the topology, tortuosity and volume fraction of the capillary system in the solid domain.

The choice of the correct diffusivity parameter to be used is mainly related to the observation scale and the nature of the solvent, the diffusive species and the media hosting the diffusion. However, since the validity of Equations 1 and 2 is general, in the following mathematical formulation the diffusivity coefficient will be generally termed D and its meaning and definition will be specified in the validation section according to the problem studied.

Substituting Equation 2 into Equation 1 gives

$$\frac{\partial C}{\partial t} = \nabla \cdot D \nabla C \,, \tag{4}$$

which is termed Fick's second law. In homogeneous materials, D is usually assumed to be a constant, i.e. independent from position, concentration and time. However, as already introduced in Section 1, HCP is composed of different hydrated and unhydrated phases, each characterized by a very different diffusion behavior, hence

$$D = D(\boldsymbol{x}) \,, \tag{5}$$

where $\boldsymbol{x}$ is the spatial coordinate vector.

2.2. Governing equations in presence of binding

Equation 4 accounts for the heterogeneous nature of the HCP, but neglects any possible chemical and physical interaction between the diffusive species and the phases in which diffusion takes place. In particular, it has been extensively demonstrated (see e.g. [1, 4, 11, 29]) that chloride ions penetrating into the HCP from the environment can interact with some hydration products, thereby modifying the diffusion process. In particular, the total concentration of chloride ions C_{tot} can be written as the sum of two terms

$$C_{tot} = C_f + C_b \,, \tag{6}$$

where C_f and C_b are the concentrations respectively of free (i.e., the ions that are free to migrate) and bound chlorides. The latter are permanently or dynamically bound to the solid phase, thus they cannot take part in the diffusion process anymore because they have become part of the solid mass of the HCP. On the other hand, the mass balance should account for the total concentration of particles C_{tot}. Hence, Equation 4 can be rewritten as

$$\frac{\partial C_{tot}}{\partial t} = \nabla \cdot D(\boldsymbol{x}) \nabla C_f \,. \tag{7}$$

Considering then the relationship

$$\nabla C_f = \nabla (C_{tot} - C_b) = \left(1 - \frac{\partial C_b}{\partial C_{tot}}\right) \nabla C_{tot} \,, \tag{8}$$

Equation 7 becomes

$$\frac{\partial C_{tot}}{\partial t} = \nabla \cdot \left[\left(1 - \frac{\partial C_b}{\partial C_{tot}}\right) D(\boldsymbol{x}) \nabla C_{tot} \right] . \tag{9}$$

It is now possible to introduce the effective diffusivity D_{eff} as

$$D_{eff}(\boldsymbol{x}, C_{tot}) = \left(1 - \frac{\partial C_b}{\partial C_{tot}}\right) D(\boldsymbol{x}) = \mu_B(C_{tot}) D(\boldsymbol{x}) \,, \tag{10}$$

where

$$\mu_B(C_{tot}) = 1 - \frac{\partial C_b}{\partial C_{tot}}\,, \tag{11}$$

is the binding activity coefficient, which makes the diffusivity coefficient dependent on the capacity of the phase hosting the diffusion to bind the diffusive species. However, as will be better explained later on, the amount of chlorides bound by the solid phase in HCP is generally expressed as a function of C_f instead of C_{tot}, i.e. $C_b = C_b(C_f)$. As a result, the binding activity coefficient as defined in Equation 11 is not readily available and, hence, a further manipulation is needed

$$\mu_B = 1 - \frac{\partial C_b}{\partial C_{tot}} = \frac{\partial C_f}{\partial C_{tot}} = \left[\frac{\partial\left(C_f + C_b\right)}{\partial C_f}\right]^{-1} = \left(1 + \frac{\partial C_b}{\partial C_f}\right)^{-1}\,. \tag{12}$$

Introducing Equation 10 into Equation 9 and accounting for Equation 12 yields

$$\frac{\partial C_{tot}}{\partial t} = \nabla \cdot D_{eff}(\boldsymbol{x}, C_f)\nabla C_{tot}\,, \tag{13}$$

that should be coupled with

$$C_f + C_b(C_f) = C_{tot}\,. \tag{14}$$

The introduction of the above non-linear equation (Equation 14) is needed since the differential field equation (Equation 13) is solved for the unknown C_{tot}, while the effective diffusivity $D_{eff}(\boldsymbol{x}, C_f)$ is a function of the free chloride concentration C_f. Once Equation 14 is solved, the binding activity coefficient $\mu_B(C_f)$ of Equation 12 can be updated to solve again Equation 13. Both Equation 13 and 14 are here solved using a Newton-Raphson algorithm.

2.3. Steady-state conditions

The diffusion process is composed of two stages: an initial transient phase where the flux of the diffusive species is established and the concentration changes in time, and a steady-state phase, where a steady flux is achieved and the variation over time of the concentration is zero.

Since the practical interest in studying chloride diffusion and chloride binding in HCP is mostly related to long-term effects (e.g., corrosion of the steel rebars and other slowly evolving phenomena), in the following steady-state conditions are assumed. In particular, the effects of the interaction between cement paste phases and chlorides on the effective diffusivity are investigated.

Steady-state conditions are enforced imposing that the time derivative in Equation 13 vanishes, thus obtaining

$$\nabla \cdot D_{eff}\nabla C_{tot} = \nabla \cdot \mu_B D \nabla C_{tot} = 0\,. \tag{15}$$

3. Binding mechanisms and related equations

Although other minor mechanisms are reported in the literature [4, 6, 30, 31], the binding of chloride ions by the hydration products in HCP follows two main mechanisms, i.e. chemical and physical interaction. Binding mechanisms, whose development is influenced by different factors [6, 32, 33], will be illustrated in detail for each phase involved in section 3.1.

The chemo-physical processes responsible for the chloride uptake are not instantaneous, but develop in time at a certain speed called binding rate [2, 11]. This rate depends on the environmental conditions and on the interacting compounds. Some authors tried to empirically calibrate the binding kinetics for the whole HCP through linear relationships, using results from diffusion tests [2]. Nevertheless, the literature available to date does not provide reliable data on the binding rate. However, it can be assumed that the binding process is fast compared to the transient diffusion phase [2], i.e. that the time needed for its full development is significantly less than that required for the establishment of the steady-state regime. Hence, it is reasonable to assume that the maximum amount of chloride ions bound for a given phase has already been reached once steady-state conditions are attained.

As reported by many authors (e.g. [6, 11, 32]), among all the hydration products present in ordinary Portland cement (OPC), only two are (almost entirely) responsible for the chloride uptake in HCP: the CSH (calcium silicate hydrates) gel and the AFm species (e.g., monosulfate hydrate), while the contributions of AFt phases (e.g., ettringite), CH (portlandite) and other hydrated or unhydrated phases are negligible under most conditions.

CSH gel is produced by the hydration of silicates (C_3S and C_2S) and is responsible for the physical binding of chloride ions [26, 34]. Conversely, the AFm presence is regulated by the amount of aluminates (C_3A and C_4AF) in the clinker, as well as the contents and forms of sulfates and carbonates [34].

3.1. Main binding mechanisms involved

Physical binding or adsorption is due to the mutual attraction between charged particles (i.e., Van der Waals forces) and is strongly related to the extent of the free CSH surface area.

Chemical binding takes place by chemical reaction [11, 32], with the presence of chloride ions leading to the formation chloroaluminate phases in preference to the conventionally formed sulfoaluminate ones structure (e.g., AFm products as $C_3A \cdot CaSO_4 \cdot 12H_2O$). For example, the chemical reaction:

$$C_3A \cdot CaSO_4 \cdot 12H_2O + 2Cl^- \rightarrow C_3A \cdot CaCl_2 \cdot 10H_2O + SO_4^{2-} + 2H_2O\,, \tag{16}$$

that produces Friedel's salt ($C_3A \cdot CaCl_2 \cdot 10H_2O$). According to Equation 16, one mole of monosulphate is able to bind 2 moles of chlorides [11], but this is a theoretical result that is reached only asymptotically because it is abstracted from the real environment

Table 1. Specific and molar masses used to convert the binding isotherms.

	Chloride Cl^-	AFm	CSH	HCP
γ $[kg/m^3]$	3.21	1990.00	2120.00	1800.00
m $[g/mol]$	35.45	622.87	228.96	-

where the reaction takes place. Chemical binding is stronger than physical binding, since it is due to chemical interactions instead of polar attraction, and is more likely to be irreversible.

3.2. Binding isotherms

The relationship between free and bound chlorides $C_b(C_f)$ at a given temperature for a defined material (single phase or HCP) is termed a binding isotherm. In the present work the isotherms proposed by Hirao et al. [11] are assumed to hold and they are converted to μg/mm^3 using the molar masses m and the specific masses γ listed in Table 1. The isotherms adopted are depicted in Figure 1a, while the $\mu_B(C_f)$ curve is shown in Figure 1b.

3.2.1. CSH gel For the CSH gel the following isotherm was proven to adequately fit the experimental results [11] (Figure 1a)

$$C_b^{CSH} = K_{CSH} \frac{a_{CSH} C_f}{1 + a_{CSH} C_f} \,, \tag{17}$$

where concentrations are expressed in μg/mm^3 and $K_{CSH} = 46.30$ and $a_{CSH} = 7.47{\cdot}10^{-2}$ are two experimentally calibrated parameters [11]. Also, following the definition of binding activity coefficient in Equation 11, the following expression is obtained for the CSH (Figure 1b)

$$\mu_{CSH} = \left[1 + \frac{K_{CSH} a_{CSH}}{\left(1 + a_{CSH} C_f\right)^2} \right]^{-1} \,. \tag{18}$$

3.2.2. AFm phase For the AFm phase a power-law isotherm was proposed in [11]

$$C_b^{AFm} = K_{AFm} {C_f}^{\alpha} \,, \tag{19}$$

where concentrations are expressed in μg/mm^3 and $K_{AFm} = 12.30$ and α=0.58 are calibrated experimentally [11]. Furthermore, from Equation 11 the binding activity coefficient is (Figure 1b)

$$\mu_{AFm} = \left(1 + K_{AFm} \alpha {C_f}^{\alpha - 1}\right)^{-1} \,. \tag{20}$$

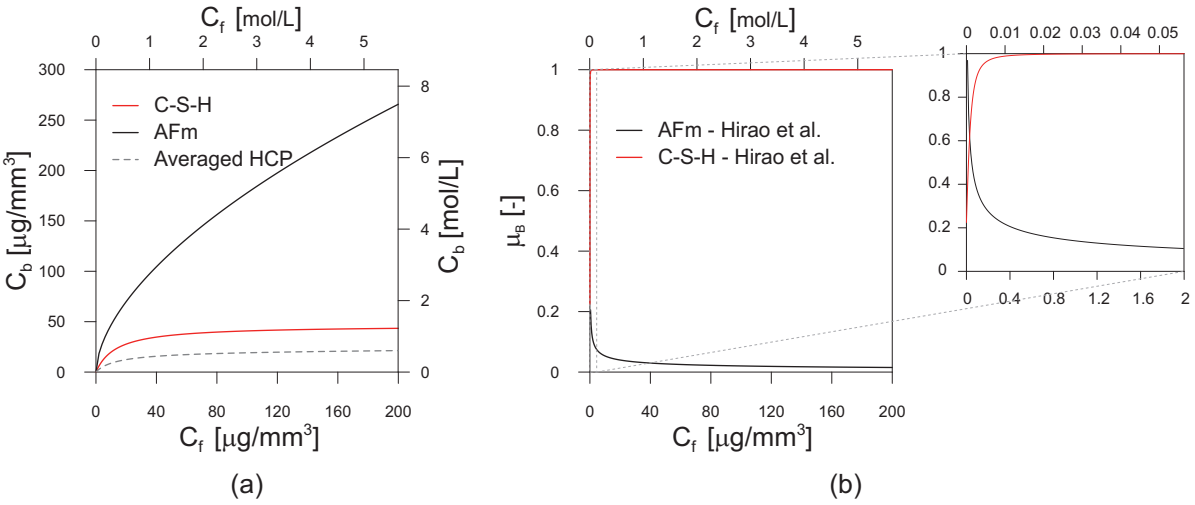

Figure 1. (a) Adopted binding isotherms (from Hirao et al. [11]) and (b) the related binding activity coefficient μ_B.

3.2.3. Averaged HCP isotherm In their work, Hirao et al. [11], proposed also an averaged relationship able to estimate the chloride bound by an HCP (Figure 1a). The proposed function is the sum of the two isotherms described in sections 3.2.1 and 3.2.2 weighted by the corresponding mass fractions

$$C_b^{HCP} = K_{CSH}\frac{a_{CSH}C_f}{1+a_{CSH}C_f}M_{CSH} + K_{AFm}C_f^{\alpha}M_{AFm}\,, \tag{21}$$

where M_{CSH} and M_{AFm} are the mass fractions of the CSH and AFm.

4. Numerical procedure

In the present work, the field equation (i.e., the mass balance in Equation 1) is discretized in space by means of the finite difference method (FDM) using a central scheme in a 3D domain. The geometry is discretized along each direction using a regular mesh of points with constant step size δ.

Since in the present work the behavior of heterogeneous microstructures of HCP is studied, it is convenient to introduce a quantity that macroscopically can describe the chloride diffusion behavior of the whole cement matrix at a larger scale than that of its single phases. This is equivalent to treating the cement paste as a homogeneous material with a homogenized diffusivity $\mathcal{D}_{eff}^{H}$ that accounts for the chloride binding. The homogenized diffusivity should be defined so as to minimize the differences in behavior between the ideally homogeneous material and the heterogeneous HCP. In the present work a least square minimization approach is adopted and the transition from the heterogeneous microscale to the homogeneous material is expressed using the following objective function

$$\Pi := \left[\langle \boldsymbol{J}\rangle - \boldsymbol{J}^{H}\left(\langle \nabla C_{tot}\rangle\right)\right]^2 \rightarrow \min\,, \tag{22}$$

where $\langle\cdot\rangle$ is the volume averaging operator defined over the heterogeneous material as

$$\langle\cdot\rangle = \frac{1}{V}\int_V \cdot \, dV \,, \tag{23}$$

and $\boldsymbol{J}^H\left(\langle\nabla C_{tot}\rangle\right)$ is the flux in the homogenized material, which is assumed dependent on the average gradient of the total concentration through the homogenized constitutive equation

$$\boldsymbol{J}^H\left(\langle\nabla C_{tot}\rangle\right) = -\mathcal{D}^H_{eff}\,\langle\nabla C_{tot}\rangle \ . \tag{24}$$

After substituting Equation 24 into Equation 22, the resulting minimization problem permits one to determine $\mathcal{D}^H_{eff}$ by solving the equation $\partial\Pi/\partial\mathcal{D}^H_{eff} = 0$, leading to

$$\mathcal{D}^H_{eff} = -\frac{\sum_i \left[\langle J\rangle_i \,\langle\nabla C_{tot}\rangle_i\right]}{\sum_i \left[\left(\langle\nabla C_{tot}\rangle_i\right)^2\right]} \,, \tag{25}$$

where $i = 1, 2, 3$ are the three orthogonal coordinate axes x, y, z.

5. Numerical simulations and comparisons with experimental results

In this section, the results of the numerical simulations are reported. First, the adopted HCP microstructures are described, then the test setups are illustrated. Finally, numerical and experimental results are compared.

5.1. HCP microstructures

Both X-ray CT scans of a real sample and simulated 3D microstructures of HCP are used here. In particular, the real CT scan is obtained from the Visible Cement Dataset (VCD) available from NIST [27, 28] while the simulated microstructures are generated using CEMHYD3D [25, 26]. The CT images from the VCD are able to distinguish only between hydration products, unhydrated residuals and pores (Figure 2a), while in the simulated HCP all the possible different phases produced during the hydration of the cement clinker are recognized. The cement powder is assumed to be composed of spherical particles whose dimensions and distribution are statistically consistent with high resolution 2D scanning electron microscope (SEM) images of the cement powder [25]. The numerical approach allows one to control each parameter of the sample volume, such as the water-to-cement ratio w/c, and the curing time t_{cur} and conditions (i.e., sealed curing or not, curing temperature). Both simulated and real microstructures used here have the same dimensions, 100x100x100 μm^3, and resolution of 1 μm^3/voxel. Concerning the FDM scheme, one node for each voxel is used.

The adopted HCP microstructure from the VCD database [27, 28], which is shown in Figure 2a, comes from the CT scan of a hydrated cement paste prepared using *Cement and Concrete Reference Laboratory Cement 133* or *CCRL133* [35] with w/c=0.45 by

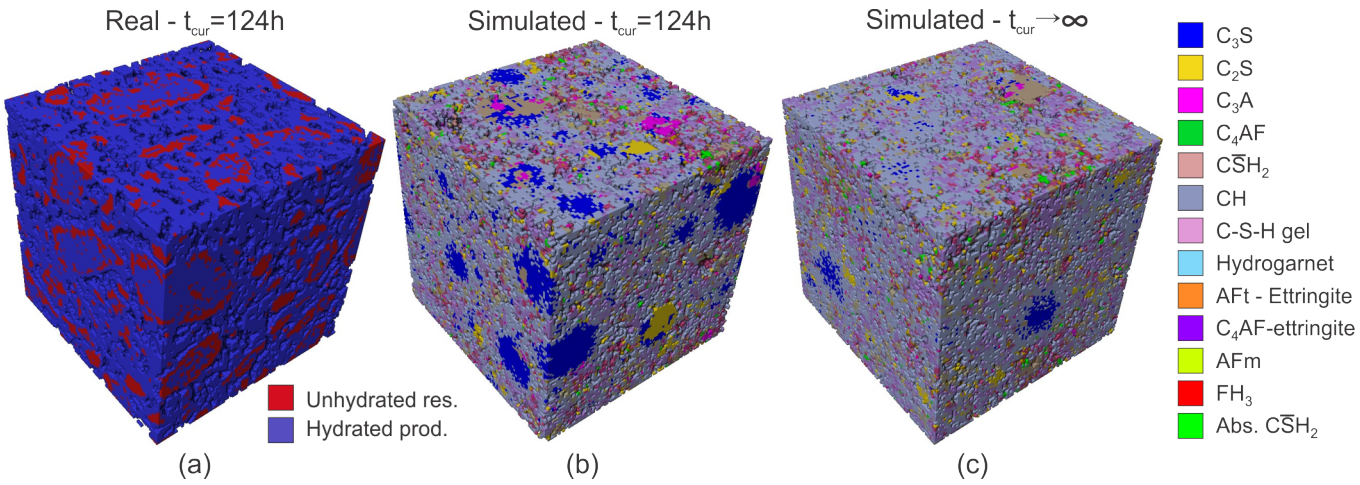

Figure 2. Voxel-based microstructures used in the numerical analyses: (a) real HCP from CT scans available at the VCD website [27, 28], (b) simulated HCP, representing the real HCP from the CEMHYD3D code [25, 26], (c) the same HCP but for an ideally infinite curing time.

mass. This is an ordinary Portland cement (OPC) with a standard composition (i.e., no additives, fly ashes, limestone or slag particles are present) and is used here for validation purposes since it is one of the most studied cements in the literature. A curing time under unsealed conditions of t_{cur}=124 h is selected because it is the longest curing time available in the VCD database [27, 28]. It is worth noting that for a curing time of 124 h, the hydration degree is about 0.63 and only a limited amount of hydration products is present (see section 5.2.6), thus the effects of binding on diffusion are not very pronounced. However, this specimen is used here to confirm that the simulated HCPs give results similar to real microstructures when studying chloride diffusion and binding.

Concerning the simulated HCPs, two different types of microstructure are used. One is meant to reproduce the real HCP adopted (i.e., $w/c = 0.45$ and cured under unsealed conditions for t_{cur}=124 h at 20 °C, see Figure 2b). The second type of HCP simulates a fully cured situation (i.e., $t_{cur} \to \infty$ in unsealed conditions at a temperature of 20 °C, see Figure 2c), and is obtained for eight different w/c ratios - namely, 0.35, 0.40, 0.45, 0.50, 0.55, 0.60, 0.70 and 0.80. For usual applications, a w/c ratio in the range 0.35-0.60 is chosen. Values greater than 0.60 are here adopted only to show the capabilities of the model. All the initial microstructures are completely flocculated, i.e. the clinker particles are randomly moved in order to obtain a single cluster of particles mutually connected (namely, a single floc [26, 36]). This choice is justified since ordinary cements, such as *CCRL133*, have a strong tendency to flocculate, unless specific additives are used [36].

5.1.1. Segmentation strategy for the real HCP microstructures The graylevel threshold values for the segmentation of the raw CT images are obtained from the graylevel

Table 2. Volume fractions and hydration degrees for the real and simulated HCPs with t_{cur} =124 h.

t_{cur} [h]	HCP type [$-$]	V_{pores} [Vol. %]	V_{hyd} [Vol. %]	V_{unhyd} [Vol. %]	α_{hyd} [-]	ν_{hyd} [-]
0	Real	59.1	0.0	40.9	0.00	-
0	Simulated	59.3	0.0	40.7	0.00	-
124	Real	28.9	56.3	14.8	0.64	2.16
124	Simulated	30.1	55.3	14.6	0.64	2.12

histogram using as a constraint the degree of hydration $\alpha_{hyd}(t)$ and the average cement stoichiometry. The degree of hydration measures the amount of cement reacted and is defined as

$$\alpha_{hyd}(t) = \frac{V_{clink} - V_{unhyd}(t)}{V_{clink}}\,, \tag{26}$$

where $V_{unhyd}(t)$ is the volume fraction of unhydrated residuals at a certain time t and V_{clink} is the initial volume of clinker (i.e., $V_{clink} = V_{unhyd}(0)$). To account for the cement stoichiometry, the following hydration expansion factor $\nu_{hyd}(t)$ is used

$$\nu_{hyd}(t) = \frac{V_{hydr}(t)}{V_{clink} - V_{unhyd}(t)}\,, \tag{27}$$

where $V_{hydr}(t)$ is the volume fraction of the hydrated products at the time t.

The segmentation thresholds are chosen in such a way as to obtain a ν_{hyd} of about 2.15, which is an average value for an OPC [26, 37], and to reproduce the degree of hydration $\alpha_{hyd}(t)$ as deduced by the CEMHYD3D simulated microstructure. The two parameters α_{hyd} and ν_{hyd} for the real and simulated microstructures are reported in Table 2, along with the volume fractions of pores, unhydrated residuals and hydrated products.

The validity of the segmentation based on the above criterion has been checked by means of the widely used Power's model [37, 38], which allows one to estimate the volume fractions of pores V^P_{pores}, unhydrated residuals V^P_{unhyd} and hydrated products V^P_{hyd} as follows

$$\begin{aligned} V^P_{pores} &= \frac{w/c - 0.36\alpha_{hyd}}{w/c + 0.32}\,, \\ V^P_{unhyd} &= \frac{0.32\,(1-\alpha_{hyd})}{w/c + 0.32}\,, \\ V^P_{hyd} &= 1 - \left(V^P_{pores} + V^P_{unhyd}\right)\,. \end{aligned} \tag{28}$$

As observable comparing Table 2 and 3 the values obtained with both CEMHYD3D and through the segmentation of the real CT images are in very good agreement with each other and with the values estimated from Power's model.

Table 3. Volume fractions for the real and simulated HCPs with t_{cur} =124 h as deduced using Power's model.

t_{cur} [h]	HCP type [−]	V^P_{pores} [Vol. %]	V^P_{hyd} [Vol. %]	V^P_{unhyd} [Vol. %]
124	Real	28.8	56.0	15.2
124	Simulated	28.1	57.3	14.6

Table 4. Volume fractions and hydration degrees of the tested HCPs with $t_{cur} =\rightarrow \infty$.

w/c	V_{pores}	V_{hydr}		V_{unhydr}	α_{hyd}
		Binding	No binding		
[−]	[Vol. %]	[Vol. %]	[Vol. %]	[Vol. %]	[-]
0.35	14.3	45.8	27.8	12.1	0.74
0.40	15.9	48.4	28.5	7.2	0.84
0.45	18.5	49.8	28.0	3.7	0.91
0.50	22.4	47.3	27.4	2.9	0.92
0.55	26.5	44.9	26.1	2.5	0.93
0.60	30.9	42.1	24.3	2.7	0.92
0.70	37.6	38.0	22.4	2.0	0.93
0.80	42.6	35.4	20.4	1.6	0.94

5.1.2. Effect of the w/c ratio on porosity and pores topology The increment of the w/c ratio is related to a higher amount of voids, as visible in Table 4, where the volume fractions for all the HCPs are listed, and in Figure 3, where the distributions of hydrated products and unhydrated residuals are also reported for different HCPs (namely, for w/c = 0.35-0.60-0.80). Figure 3 also shows that, passing from w/c = 0.35 to 0.60, the voids network is more extended but topologically similar, meaning that it keeps the characteristic of capillarity (i.e., the presence of small voids connected by capillaries). Conversely, for the HCP with w/c = 0.80 an alveolar-like structure characterized by large cavities forming preferential pathways for the diffusion is present. However, these cavities are connected by capillaries that obstruct ions migration.

5.1.3. Percolation of the pore network Another factor strongly related to the diffusive behavior is the percolation of the pore network (see [7, 8] for a detailed review). A system of voids is termed percolated in a certain direction if, in that direction, there exists at least one continuous path that goes from one end to the opposite one. If such a path does not exist, the pore network is said to be depercolated. In the latter case, the ions should overcome membranes of solid material that isolate the capillary pores in clusters, delaying the diffusion [8]. Garboczi and Bentz [8] demonstrated that the depercolation limit for a Portland HCP corresponds to a void volume fraction of 18 %,

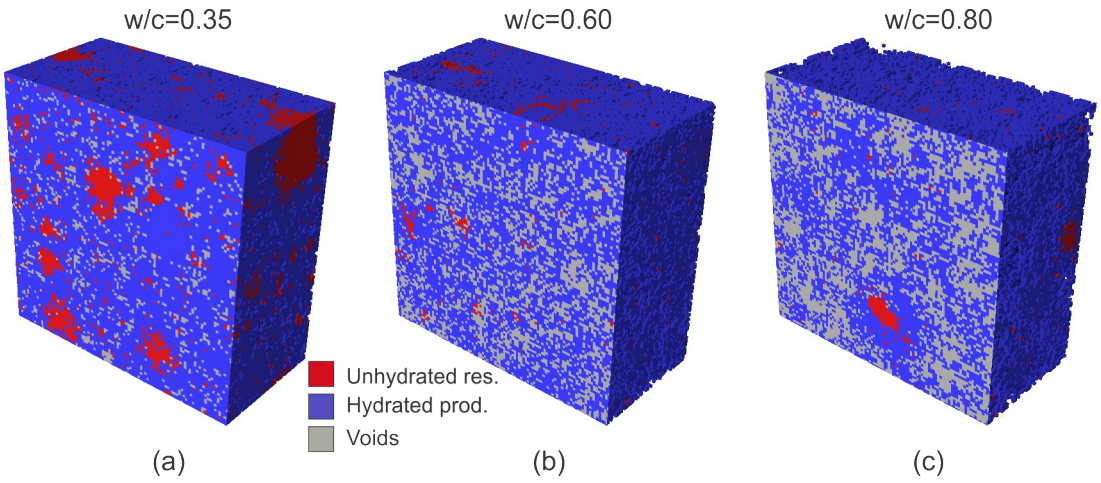

Figure 3. Sections of the simulated microstructures used for the diffusion test showing distribution of hydration products, unhydrated residuals and voids: (a) w/c=0.35, (b) w/c=0.60, (c) w/c=0.80.

using a pore resolution of 1 μm in the model. Above this limit the probability to find a percolated pore system in an ideally infinite domain is 100 %, while below this limit such probability is 0 %. In this latter case, the HCP microstructure contains many depercolated subpaths and isolated clusters of pores. The former are pore systems that can be directly accessed from one of the outer exposed surfaces, while the isolated pores can be reached by diffusing species only after passing through a region of solids. The extent in volume of the percolated, depercolated and isolated pores, the presence of bottlenecks in the percolation path and its tortuosity strongly influence the diffusive behavior of the HCP [10].

The changes in the capillary pore network are observable in Figure 4, where the evolution of the percolated and depercolated pore systems for the HCPs with w/c=0.40-0.45-0.50 is examined using a burning algorithm similar to the one proposed by Bentz and Garboczi in [7]. In particular, it is shown that, for the HCPs used here, 0.45 is the lowest w/c that produces a percolated path, which however is limited in extension and characterized by the presence of bottlenecks and a high tortuosity (Figure 4b). Conversely, the microstructure with w/c=0.40 is depercolated (Figure 4a) and the one with w/c=0.50 has already a very large percolated system.

Figure 5 reports the percolated, depercolated and isolated fractions of the total pore volume as functions of the w/c ratio for fully cured systems. It can be seen how the pore connectivity changes with the w/c ratio, confirming that below a pore volume of nearly 18 % (i.e., for $w/c \leq 0.40$) the microstructures are depercolated while for $0.45 \leq w/c \leq 0.60$ the extension of the percolated system grows rapidly, then for $w/c >$ 0.60 the curve flattens until reaching a value of about 93 % at w/c=0.80. The aforementioned burning algorithm is applied also to the samples with t_{cur}=124 h resulting in a percolated void fraction of 79.8 % and 99.1 % respectively for the simulated and real microstructure. These results are obviously higher than their fully hydrated coun-

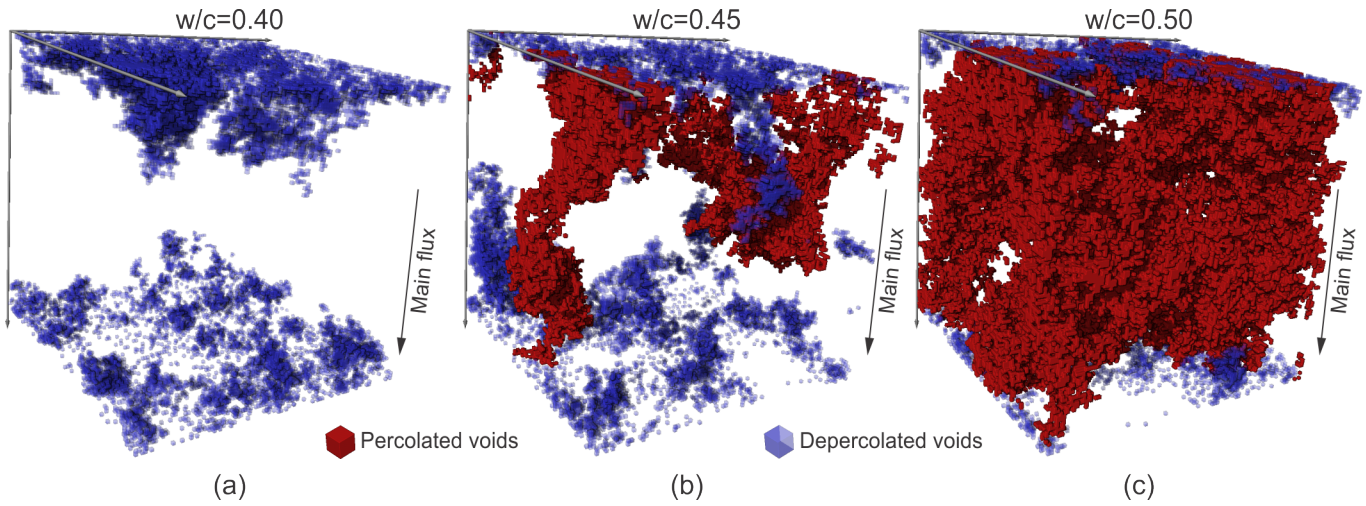

Figure 4. Percolated and depercolated pathways determined using a burning algorithm for different HCPs: (a) w/c=0.40, (b) w/c=0.45 and (c) w/c=0.50.

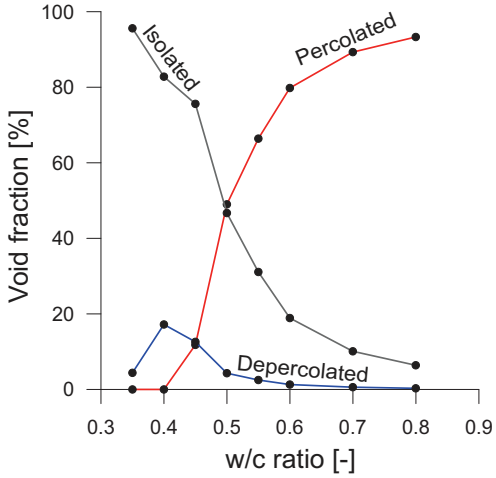

Figure 5. Percolated, depercolated and isolated fractions of the total pore volume.

terparts because of the limited curing time, however they are in good agreement with those reported in [37] for a similar case. Although it is recognized that the chosen voxel resolution will influence both the percolation of the capillary porosity and the resulting diffusivity [39], in this study, the resolution for the simulated microstructures was set to 1 μm^3/voxel, following the results of previous studies where simulated microstructures are compared to experimental CT images [40]. Furthermore, the adopted resolution matches the one of real microstructures of the VCD database [27, 28].

5.1.4. Comparison between real and simulated HCPs In Figure 6 the real and simulated microstructures of the non-hydrated cement clinker used here are compared and the corresponding volume fractions are reported in Table 2. Although the real geometry is composed of highly irregular clinker particles while the simulated ones are spherical,

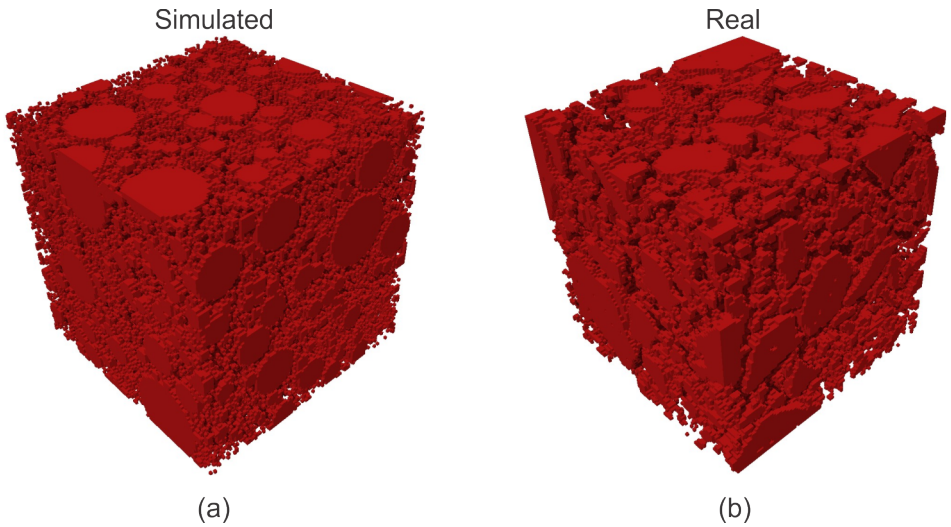

Figure 6. Clinker (non-hydrated cement powder) 3D microstructures: (a) simulated using CEMHYD3D [25, 26], (b) from CT scan images (from VCD [27, 28]).

a good agreement is noticeable, especially concerning the presence and distribution of both large and small clinker particles.

Similar conclusions can be drawn comparing the real and simulated (hydrated) HCPs depicted in Figure 7. In particular, as also reported in [37], the microstructures appear similar even though the geometry coming from the CT scan images (Figure 7b) is more irregular than the simulated counterpart (Figure 7a). However, for the real HCP only a coarse subdivision of the phases is available (i.e., voids, hydrated products and unhydrated residuals) because of the limits of the 3D imaging techniques available at that date. Conversely, although in the simulated microstructures the geometry is idealized, all the different phases present in HCP are finely resolved with a precision of 1 μm^3. Moreover, the simulation model used [25, 26] allows one to directly and easily control all the principal parameters of a cement clinker and of a HCP.

In Table 2 the volume fractions of voids, hydrated products and unhydrated residuals for the real and simulated microstructure used herein are reported. The marginal differences in the values are possibly related to the fact that the w/c ratio in the simulated microstructures is directly enforced on the tested sample, while in the real HCP it is imposed on the whole volume from which the sample is extracted, that is much larger than 100x100x100 μm^3.

In [37], for a cement similar to the one analyzed here, hydrated and clinker microstructures from CT scan images and generated via CEMHYD3D adopting both spheres and real irregular particles are compared. The author demonstrated that the employment of spherical geometries does not affect the phase distribution in microstructures with the same w/c ratio, provided that a reliable particle size distribution is given [37].

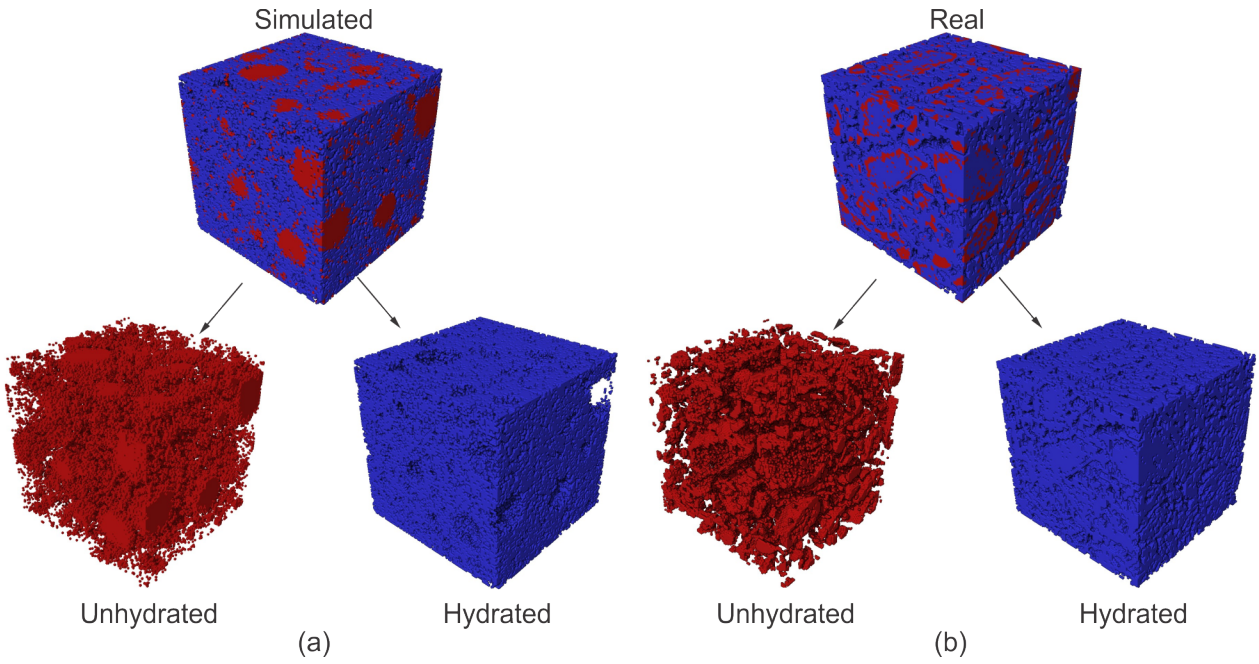

Figure 7. HCPs with t_{cur}=124 h used in the numerical simulations and their hydrated products and unhydrated residuals: (a) simulated using CEMHYD3D [25, 26], (b) from CT scan images (from VCD [27, 28]).

5.2. Numerical simulations of diffusion and binding

The diffusion test is performed by prescribing a concentration gradient between two opposite faces of a sample. By tracking the amount of chloride ions reaching the outlet face, the diffusion coefficient of the HCP is estimated [29, 41, 42]. The most classic setup involves an HCP sample where at one face (inlet face) a chloride concentration C_{inlet} is applied, while the opposite face (outlet face) is in contact with a solution with concentration C_{outlet} equal to zero (i.e., pure water). All the other faces are sealed, i.e. the chloride flux normal to the surface is zero. Differently, the binding test involves the application of a fixed time-invariant concentration of chlorides on all the faces of the specimen (i.e., the sample is immersed in a chloride bath) and is used to test the binding capability of the HCP [11]. By testing several samples at different concentrations, the isotherm curve for the tested HCP is obtained.

In the following, after the definition of the parameters adopted in the performed analyses, the numerical results are compared to experimental results for the diffusion tests of Page et al. [29], Yu and Page [41], Nagala and Page [43], MacDonald and Northwood [44] and Tang and Nilsson [42] along with the binding tests of Hirao et al. [11]. Also, some observations arising from the comparison between real and simulated HCPs are drawn.

5.2.1. Diffusion coefficients of the HCP phases As already outlined in section 2.1, the proposed model accounts for the heterogeneity of the values of the diffusivity in the

HCP microstructure. Therefore, the diffusivity parameter in Equation 2 (and, hence, in Equation 4) is here written as

$$D(\boldsymbol{x}) = \sum_h D_h \delta_{h,k(\boldsymbol{x})} \,, \tag{29}$$

where the summation is evaluated over all the possible phases h with diffusivity D_h present in the microstructure, $k(\boldsymbol{x})$ is the phase at the point $\boldsymbol{x}$, and $\delta_{h,k(\boldsymbol{x})}$ is the Kronecker delta evaluated at that point, which is equal to 1 if $k(\boldsymbol{x}) = h$ and 0 otherwise. Because of the reduced dimension of the voids in the HCP (transparent in Figure 2), a value for the diffusivity of chloride ions in capillary pores (see Section 2) $D_c = D_{pores} = 3.0{\cdot}10^{-10}$ m^2/s at room temperature (T=20°C) is assumed, in very good agreement with values proposed by other authors [17, 29]. Conversely, for all other phases the solid diffusivity D_s should be adopted. In this case the diffusivity is much lower than in pores because, although in the solid material a capillary network is still present because of the agglomeration of crystals, the diameter of the micropores is much smaller and the tortuosity is higher. Moreover, D_s accounts also for the part of the volume effectively occupied by the crystal grains. For the diffusivity of the phases exhibiting binding (CSH and AFm), the well accepted empirical formula proposed by Garboczi and Bentz [8] $D_{bind} = D_{AFm} = D_{CSH} = D_{pores}/400$ is adopted here for both CSH and AFm, although it is recognized that they are two different hydration products. This assumption is needed since it is not possible to find in the literature a reliable experimental estimation of such parameters. According to the literature, all other hydrated or unhydrated phases show a lower diffusivity than these binding phases, hence here a value of $D_{NObind} = D_{unhydr} = D_{bind}/10 = D_{pores}/4000$ is assumed in order to account for the presence of nanopores smaller than a fraction of micron. The nanopore network arises from the imperfect coalescence of different grains of the solid phase. Concerning the real microstructure, D_{unhydr} is associated with all unhydrated residuals, while for the hydration products it is assumed that their volumetric composition is voxel-wise equal to the hydration products composition of the simulated HCP, which is composed at t_{cur}=124 h by 59.5 % of CSH and by 1.0 % of AFm while the remaining part is composed of non-reactive phases. Then, following the additivity of Equation 29, the hydrated diffusivity is taken as the weighted average of the respective diffusivities, i.e. $D_{hydr} = (0.595 + 0.010)D_{bind} + (1 - 0.605)D_{NObind}$. The same approach is used to define the binding curve of the hydration products in the real HCP, namely $C_b^{hydr} = 0.595 C_b^{CSH} + 0.010 C_b^{AFm}$, while the binding coefficient follows the relationship of Equation 12. All the adopted parameters are summarized in Table 5. The low amount of AFm crystals is justified by the short curing time (124 h). In CEMHYD3D the AFm phase forms from the ettringite products (AFt) after the complete sulphate depletion [25, 26], hence the AFm volume fraction increases by about a factor of 3 for a fully hydrated microstructure (Sect. 5.2.5).

5.2.2. Numerical simulation of the diffusion tests Two series of tests are here reproduced whose main difference is the imposed chloride concentration at the inlet

Table 5. Diffusion coefficients used in the numerical simulations.

D_{pores} $[10^{-12}\,m^2/s]$	$D_{bind} = D_{CSH} = D_{AFm}$ $[10^{-12}\,m^2/s]$	D_{NObind} $[10^{-12}\,m^2/s]$	D_{unhydr} $[10^{-12}\,m^2/s]$	D_{hydr} $[10^{-12}\,m^2/s]$
300.000	0.750	0.075	0.075	0.480

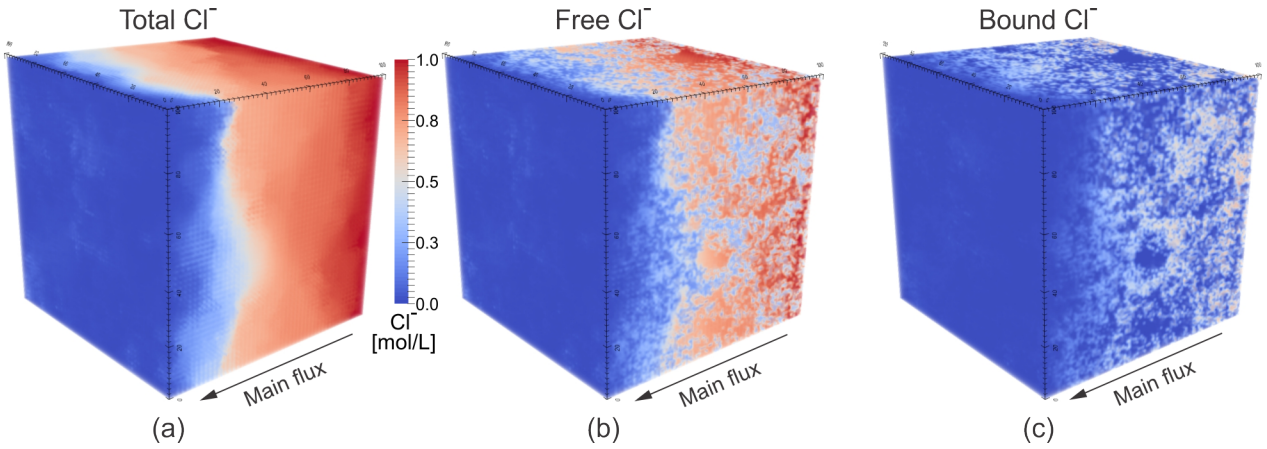

Figure 8. Steady-state chloride concentrations from the numerical simulation of the Page et al. [29] test for the simulated HCP with $t_{cur} \to \infty$ and w/c=0.45: (a) total chloride concentration, (b) free chloride concentration, (c) bound chloride concentration.

face, which is C_{inlet}=1.0 mol/L for Refs. [29, 41, 43, 44] and C_{inlet}=0.5 mol/L for Ref. [42]. For both, the outlet concentration is C_{outlet}=0 mol/L and the flux normal to all the other faces is set to zero.

In Figure 8, the results for C_{inlet}=1.0 mol/L in terms of total, free and bound chloride concentrations for the specimen with w/c=0.45 and $t_{cur} \to \infty$ are presented, while the results for the other specimens are qualitatively very similar. It is evident that, although the total chloride concentration distribution appears quite smooth (Figure 8a), the opposite is true for the free and bound chloride distributions (Figure 8b-c). This is due to the heterogeneous distribution of the hydration products (Figures 2c) and to the presence in the clinker structure of large particles that are hydrated only in their outer part, leading to the formation of clusters of unhydrated residuals as visible in the side face of the HCP in Figure 8b-c.

The results of all the diffusion test simulations in terms of homogenized diffusivity both accounting for and neglecting the binding effects, respectively $\mathcal{D}^H_{eff}$ and $\mathcal{D}^H_{NObind}$, are reported in Table 6 and illustrated in Figure 9. Moreover, in Figure 10 the influence of the binding effect on the homogenized diffusivity $\mathcal{D}^H$ is expressed through the ratio $\rho_{\mathcal{D}}$ defined as

$$\rho_{\mathcal{D}} = 1 - \frac{\mathcal{D}^H_{eff}}{\mathcal{D}^H_{NObind}}\,. \tag{30}$$

Table 6. Results of the numerical simulations of the diffusion tests.

HCP type	w/c [−]	t_{cur} [h]	$\mathcal{D}^H_{eff}$ [$10^{-12}\,m^2/s$] 0.5 mol/L$^{(a)}$	$\mathcal{D}^H_{eff}$ [$10^{-12}\,m^2/s$] 1.0 mol/L$^{(a)}$	$\mathcal{D}^H_{NObind}$ [$10^{-12}\,m^2/s$]
Simulated	0.35	$\to\infty$	0.46	0.52	1.12
Simulated	0.40	$\to\infty$	0.70	0.79	1.46
Simulated	0.45	$\to\infty$	1.17	1.30	2.29
Simulated	0.50	$\to\infty$	2.97	3.14	4.50
Simulated	0.55	$\to\infty$	6.94	7.15	8.62
Simulated	0.60	$\to\infty$	13.42	13.67	15.22
Simulated	0.70	$\to\infty$	28.35	28.54	30.07
Simulated	0.80	$\to\infty$	44.26	44.42	45.66
Real CT scan	0.45	124	-	17.90	18.70
Simulated	0.45	124	-	13.09	14.31

$^{(a)}$ Values related to the inlet concentration C_{inlet}.

From the numerical results in Figure 9 it is possible to notice how an increase of the w/c ratio leads to an exponential increase of the homogenized diffusivity that approaches a linear trend for $w/c > 0.6$ (Figure 9 and Table 6). For very high w/c ratios the homogenized diffusivity $\mathcal{D}^H$ grows rapidly approaching D_{pores}, which is the expected value in the ideal case of $w/c = \infty$. As already reported by Garboczi and Bentz [8], such non-linear trend is related to the increment, with the w/c ratio, of the volume of the capillary pores (see Table 4 and section 5.1.2), which have a diffusivity value 2-3 orders of magnitude higher than that of the other phases (Table 5). Hence, even a relatively small increase in pore volume can result in a relevant increment of the homogenized diffusivity.

As already outlined in section 5.1.2, the increment of porosity leads to a change in the pores topology that, interestingly, takes place in correspondence of the beginning of the linear branch of the $\mathcal{D}^H - w/c$ curve (Figure 9), i.e. for $w/c \simeq 0.60$ for the cement used here.

The sudden change in slope of the $\rho_D - w/c$ curve for $w/c \simeq 0.45$ (Figure 10) can be explained considering the percolation properties of the HCP microstructures (section 5.1.3). Table 4 and Figure 5 show that such slope change takes place in correspondence of the transition from the percolated to the depercolated HCPs (Figure 4). Depercolation leads to a dramatic reduction of the pore network connectivity delaying the penetration of chloride ions. Moreover, as visible in Figure 3a and in Table 4, for low w/c ratios a larger amount of unhydrated residuals are still present especially in correspondence of large clinker particles. In such cases, part of the cement does not react with water leading to the formation of inclusions of unhydrated products, which are assumed not to bind chlorides.

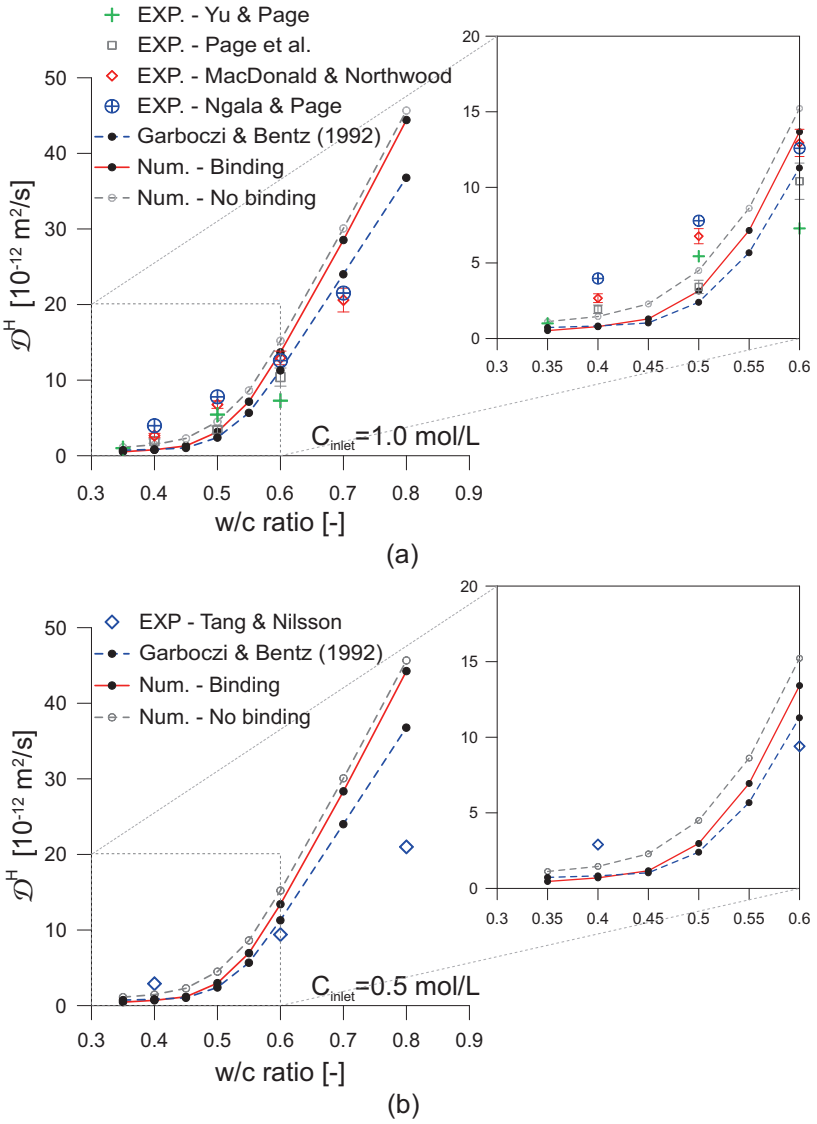

Figure 9. Homogenized diffusivity vs. w/c ratio curves from the numerical analyses of the diffusion tests: (a) tests with C_{inlet}=1.0 mol/L, (b) tests with C_{inlet}=0.5 mol/L.

Although in Figure 9 the difference between homogenized diffusivity with and without binding is apparently limited, the parameter $\rho_{\mathcal{D}}$ plotted in Figure 10 shows that the interaction between solid phases and chloride ions indeed plays a significant role in the diffusive behavior. For the values of w/c commonly employed (i.e. in the range 0.35-0.60), a reduction of the homogenized diffusivity in the range 10 %-60 % is observed. Such a relevant influence is due to the small values assumed by the binding activity coefficients μ_B within the HCP volume in the phases exhibiting binding, as also illustrated in Figure 11.

Figure 10 and Table 6 show that for $w/c > 0.60$ the difference between homogenized diffusivity with and without binding is less than 10 % even though the solid phase is mainly composed of hydration products exhibiting binding, as also reported in Table 4.

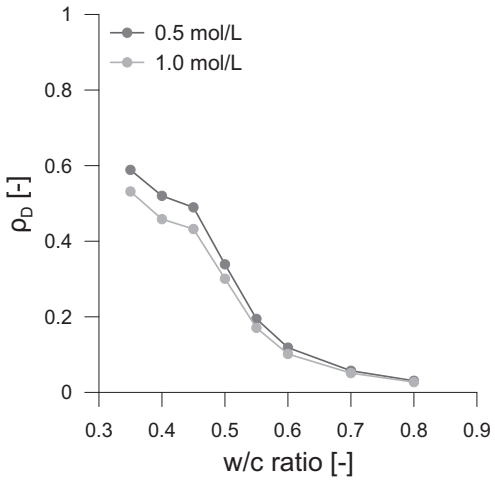

Figure 10. Influence of the binding effect on the homogenized diffusivity ($\rho_{\mathcal{D}}$ ratio) for varying w/c ratio from the numerical analyses of the diffusion tests.

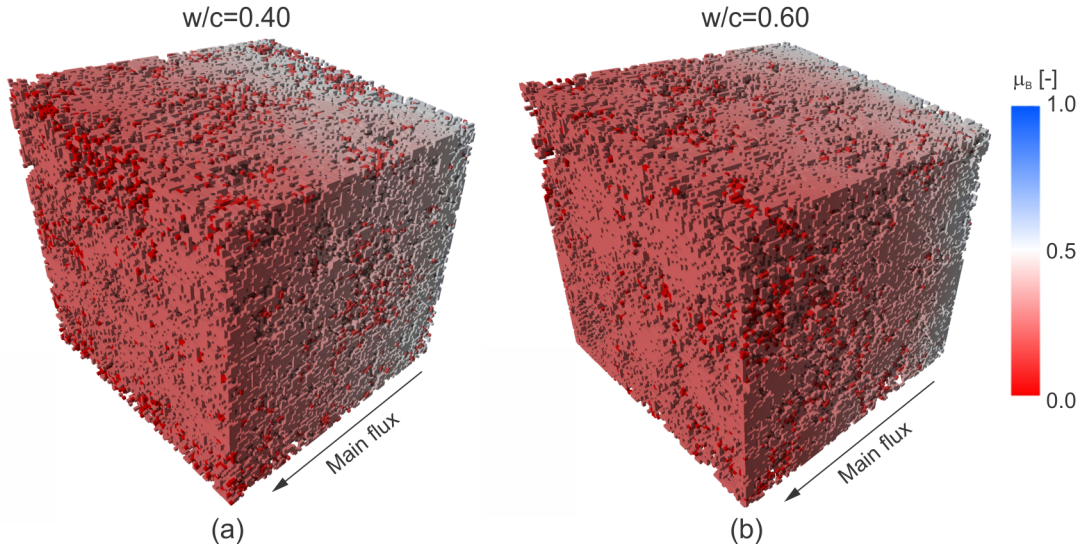

Figure 11. Maps of the calculated diffusivity activity coefficient μ_B for the phases showing binding for the simulated microstructures with (a) w/c=0.40 and (b) w/c=0.60.

This is due to the decreased volume of solid phase with respect to the capillary pore network, whose volume fraction is well above the percolation limit [8]. In such cases the alveolar-like void structure dominates the diffusion process because of the high pores diffusivity and, at the same time, the global effect of binding is reduced since binding does not take place in water saturated pores. This leads to a drastic change in the diffusion process, confirming the preeminent role of the voids in the diffusion process for HCPs with a volume fraction of capillary pores much higher than the percolation limit [8].

The influence of binding is less pronounced in the specimens with limited curing

time t_{cur}=124 h than for fully hydrated pastes (see Table 6) because the progression of the hydration process implies more hydration products exhibiting binding and, thus, its effect becomes more prominent in later age specimens, as will be also illustrated in section 5.2.6. Moreover, the value of the homogenized diffusivity appears inversely related to the curing time (Table 6). This happens because the hydration process reduces drastically the amount of capillary voids in HCP and, as already noted, increases the amount of hydration products that exhibit binding. These two effects both lead to a reduction of the diffusivity with further hydration.

5.2.3. Comparison with the experimental results of the diffusion tests Figure 9 also compares the numerical results with the experimental data [29, 41–44]. A reasonable agreement is observable between the test results and the numerical curves accounting for binding for both C_{inlet}=1.0 mol/L (Figure 9a) and C_{inlet}=0.5 mol/L (Figure 9b). However, the difference between the cases with and without binding is very close to the deviation between the various sets of the experimental results. The latter deviation appears quite high, but this is not too surprising considering that the various series of tests used involve different types of cement clinker, temperatures, specimen dimensions and test setups. Such effects may significantly modify the value of the pore diffusivity D_{pores} and, hence, all the diffusivity parameters. Unfortunately, the literature does not report, to date, enough information to allow for a precise and detailed calibration of the diffusivity parameters accounting for all the possible phenomena influencing diffusion. Hence, as also mentioned in section 5.2.1, the parameters adopted here are not finely tuned for the cases at hand. Furthermore, the values of D_{pores} present in the literature are usually deduced neglecting the binding effect, most of the time trying to best fit a simplified solution of Fick's equation with a set of experimental results. It is finally worth noting that, accounting only for the range of w/c ratio commonly used (i.e., $w/c < 0.60$) and for data from the same experimental campaign, the deviation becomes much smaller. Certainly a proper case-wise calibration of the parameters would give better agreement with a specific dataset but this is not the goal of the present work. The present comparison should be conceived as a general validation aimed at demonstrating that the model proposed is able to capture, adopting both simulated and real microstructures, the main processes governing diffusion at the microscale as well as the effects of the main variables involved.

As expected, the numerical results in the range $0.35 \leq w/c < 0.60$ always lie below the experimental points. This behavior is reasonable considering that the experimental tests were performed with $t_{cur} < \infty$ and that the homogenized diffusivity $\mathcal{D}^H$ decreases with the progress of the hydration. From Figure 9 it is also evident that, for very porous HCPs (i.e., for $w/c \geq 0.60$), the homogenized diffusivity is overestimated. However, heterogeneous specimens are likely to be produced for so highly porous HCPs, because of the presence of large cavities inducing phenomena such as bleeding and/or sedimentation. Also, as noted before, for microstructures with $w/c > 0.60$ the diffusion mechanism can be completely different from Fickian diffusion because of the changes in

the topology and percolation characteristics of the capillary pore network (Figures 3, 4 and 5). In particular, the increment in pores dimension might promote the presence of convective contributions to the particles motion.

It is worth noting that, following what reported in [11], there is the possibility that, under particular conditions, also the AFt (ettringite) reacts with chloride ions producing Friedel's salt following a mechanism similar to AFm. Accounting for the AFt products as reactive phases with a binding isotherm given as in Eq. 19 the changes in the final results are limited, in the order of about 0.5-1 %. However, the role of AFt in the binding process is still controversial and is not accounted for henceforth.

The aforementioned different behavior for porous HCPs is also implicitly considered in the semi-empirical relationship based on the percolation theory proposed by Garboczi and Bentz [8] that, according to the authors, can be adopted to characterize HCPs with $w/c \leq 0.60$. The formula, which is reported for comparison in Figure 9, reads

$$\frac{\mathcal{D}^H}{D_{pores}} = 10^{-3} + 0.07\left(\frac{V_{pores}}{100}\right)^2 + h\left(\xi\right)\left[1.8\xi^2\right] \quad \text{with} \quad \xi = \frac{\mathrm{V_{pores}}}{100} - \frac{\mathrm{V_c}}{100}\,, \tag{31}$$

where all the volume fractions are expressed in percentage, V_c= 18 % is the percolation threshold for an OPC [8] and $h(\xi)$ is the Heaviside step function, which is equal to 0 when $\xi \leq 0$ and 1 if $\xi > 0$.

The obtained numerical results are generally in good agreement with Equation 31 (Figure 9) confirming the reliability of the model proposed and the leading role of the pore percolation. In particular, note that the range of validity of Equation 31 corresponds to the range of w/c ratios where the proposed approach is more accurate, and, within this applicability range (i.e., for $w/c \leq 0.60$), the agreement between the proposed approach and the experimental data is similar to the one achieved with Equation 31 (Figure 9). However, Equation 31 is based on best fitting procedures and does not directly account for binding and for the heterogeneous distribution of the various phases, meaning that it cannot be generalized.

5.2.4. Comparison with analytical bounds Figure 12 illustrates the comparison of the numerical and experimental results with analytical homogenization bounds obtained neglecting the binding behavior, including the Voigt, Reuss, Voigt-Reuss-Hill (VRH), Hashin-Shtrikman upper, lower and average bounds (respectively HS+, HS-, Avg. HS). Analytical bounds are very large and also their average values (VRH and Avg. HS curves Figure 12) are usually significantly higher than the experimental results, demonstrating that the adoption of a numerical approach is mandatory to achieve reasonable accuracy.

5.2.5. Numerical simulation of the binding tests Simulating the binding tests in [11] (i.e., imposing to all the six faces of the specimen the same concentration), it is possible to obtain the numerical binding isotherms, which are reported in Figure 13 for the HCPs with w/c of 0.40 and 0.60. The same plot also contains the average curve proposed by Hirao et al. [11] (Equation 21), where the mass fractions for the two specimens

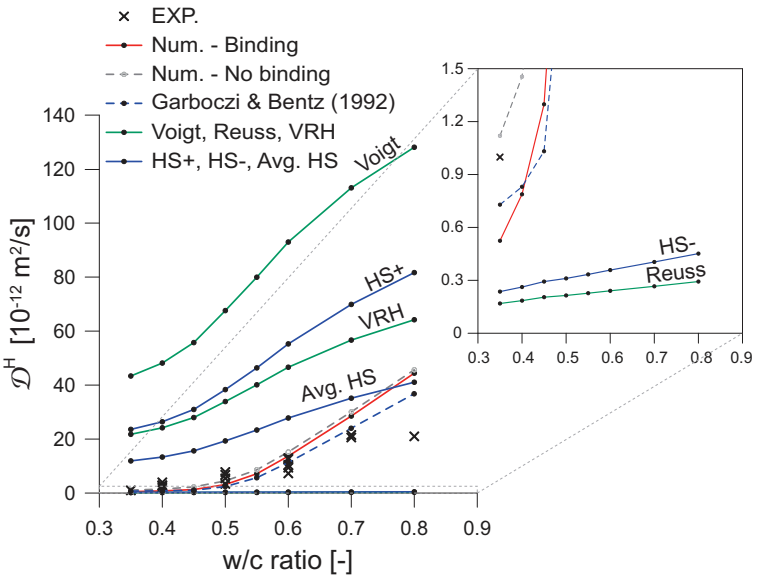

Figure 12. Comparison between the homogenized diffusivity from experimental results, numerical results and various analytical bounds, such as Voigt bound, Reuss bound, Voigt-Reuss-Hill bound (VRH), Hashin-Shtrikman upper, lower and average bounds (respectively HS+, HS- and Avg. HS).

Table 7. Fractions of the binding phases for w/c=0.40 and 0.60.

w/c	*AFm*		*CSH*	
	Vol. %	Mass %	Vol. %	Mass %
0.40	2.90	3.25	45.42	53.49
0.60	2.05	2.27	40.11	47.25

are estimated from the respective fully cured simulated microstructure (Table 7) using the phases and HCP characteristics reported in Table 1. The numerical simulations show a lower amount of bound chloride ions when compared with the prediction of the empirical averaged relationship of Hirao et al. [11]. These differences can be explained considering that in Hirao et al. [11] it is implicitly assumed that the concentration of the free chlorides is uniform in all the phases (voids, hydrated products and unhydrated residuals) while the numerical curves reported in Figure 13 are the volume average of the whole HCP, where the free chloride concentration is not homogeneous because of the effects of the binding. Accounting for the aforementioned issues, the agreement is acceptable.

5.2.6. Comparison between the diffusive behavior of real and simulated HCP In Figures 14 and 15 the contour maps of the total, free and bound chloride concentration respectively for the simulated and real microstructures with t_{cur}=124 h and w/c=0.45 are reported. Despite the different starting particle geometry, the two images show a good agreement, both qualitatively and quantitatively. The slight overestimation of

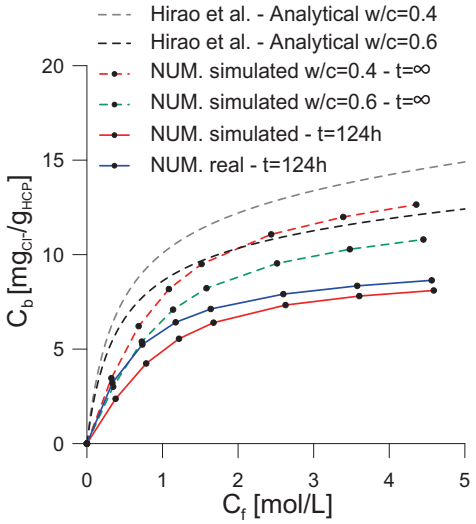

Figure 13. Binding curves from the numerical simulations of the binding tests.

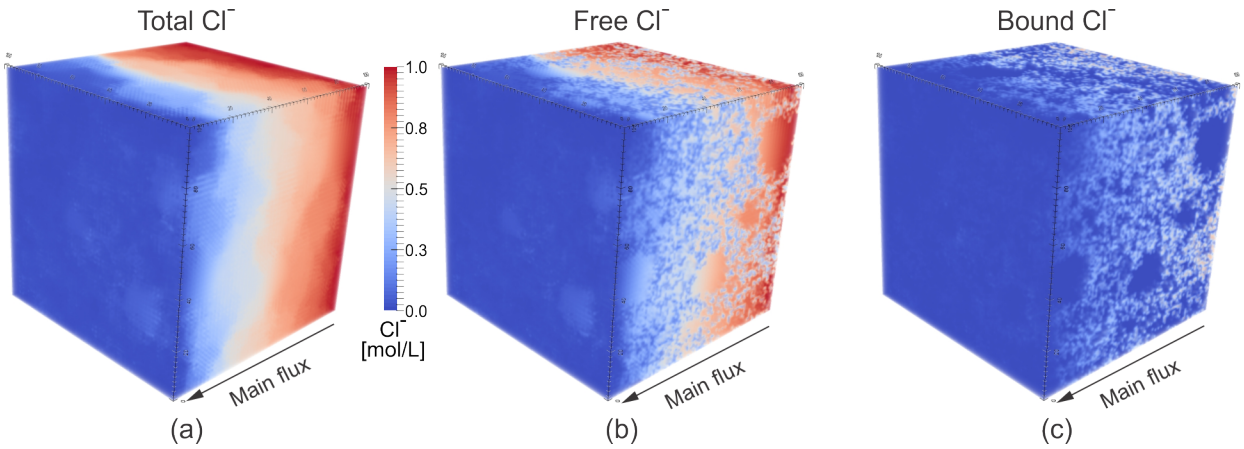

Figure 14. Steady-state chloride concentrations from numerical simulation of the test with C_{inlet}=1 mol/L for the simulated HCP with t_{cur}=124 h and w/c=0.45 reproducing the CCRL133 cement [27, 28]: (a) total chloride concentration, (b) free chloride concentration, (c) bound chloride concentration.

the homogenized diffusivity noticeable in Table 6 for the real microstructure agrees with the differences in the volume fraction of the percolated pore network. However, such difference is also partly due to the assumed relationship for the diffusivity and the binding isotherm described in section 5.2.1. In particular, the adopted hydration products diffusivity is weighted on the volume fractions of the various hydration products constituting thus an upper bound value (namely, a Voigt bound). Moreover, the binding isotherm for hydration products is calculated on a volume average basis as well, limiting thus the possibility to reach values of μ_B close to zero because of the presence of phases that are insensitive to the binding process.

Concerning the binding test Figure 13 demonstrates that the behavior of real and simulated microstructures is very similar. The difference in the amount of chlorides

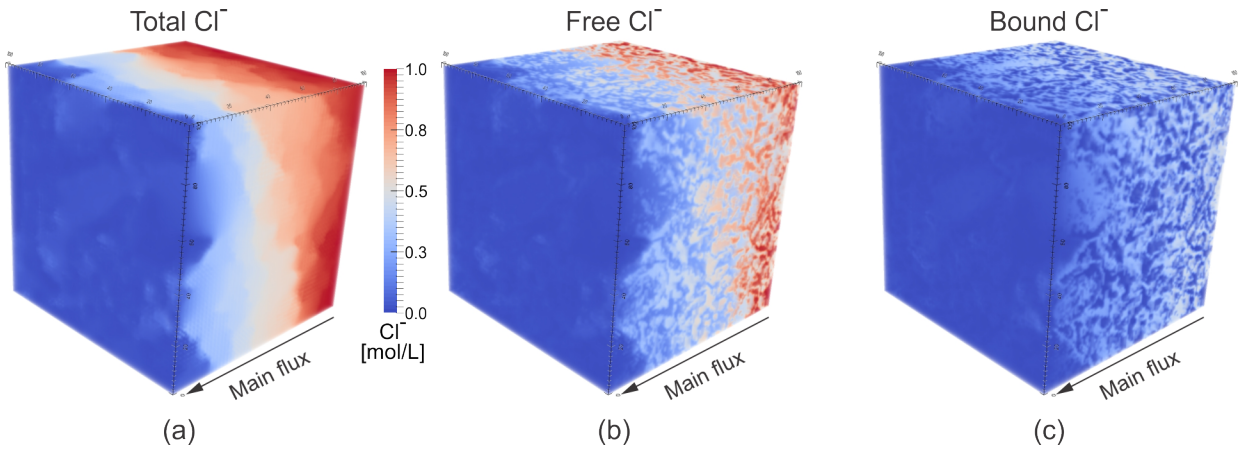

Figure 15. Steady-state chloride concentrations from numerical simulation of the test with C_{inlet}=1 mol/L for the real CCRL133 [27, 28] HCP with t_{cur}=124 h and w/c=0.45: (a) total chloride concentration, (b) free chloride concentration, (c) bound chloride concentration.

bound is probably due to the distribution of the phases exhibiting binding, that are lumped in all the hydrated products in the real microstructure, while they are pointwise identified in the simulated one (Figure 2).

The above evidence makes it possible to conclude that, for the steady-state chloride diffusion behavior, the results of simulated and real HCP microstructures show a good agreement provided that for the latter a sufficiently precise estimate of the volume fractions of the phases exhibiting binding is available.

6. Conclusions

The problem of diffusion of chloride ions into hardened cement paste (HCP) at the microscale level is addressed. The microstructures of the HCP are obtained through computer tomography (CT) images of a real sample as well as simulated using CEMHYD3D. A model is proposed based on steady-state Fickian diffusion accounting explicitly for the binding effects through the introduction of a binding activity coefficient deduced by means of binding isotherms. The model, implemented with the finite difference method, is validated with respect to diffusion and binding tests by means of comparisons with experimental results. Based on the obtained results, the following conclusions can be drawn:

- the proposed model provides a satisfactorily accurate prediction of the diffusivity of ordinary Portland cement (OPC) with $0.35 \leq w/c \leq 0.60$, especially considering that no fine tuning of the parameters is performed. In particular, the magnitude of the predicted diffusivities and their trend vs. the w/c ratio are consistent with different datasets from the literature;
- the effect of binding in OPC with $w/c \leq 0.60$ is non negligible and may reduce the homogenized diffusivity of the HCP by up to 60 %;

- the heterogeneous nature of the microstructure due to the distribution of the phases in HCP plays a significant role in the diffusion of chlorides, especially including the binding effect. The key role of the percolation properties of the HCP capillary pore system is confirmed;
- the adoption of the Fickian theory leads to an overestimation of the homogenized diffusivity for very porous HCP (i.e. for $w/c > 0.60$), suggesting a drastic change in the diffusive process in relation to the pore topology;
- although further validation adopting different cements and w/c ratios is advisable, the first results of simulated and real HCP microstructures show a good agreement provided that for the latter a sufficiently precise estimate of the volume fractions of the phases exhibiting binding is known.

Acknowledgments

This research was founded by the European Research Council under the European Union's Seventh Framework Programme (FP7/2007-2013)/ERC Grant agreement n. 279439 and by the German DFG project Graduiertenkolleg 2075 (GRK-2075).

References

[1] Bentz D P and Garboczi E J 1993 A computer model for the diffusion and binding of chloride ions in Portland cement paste - NISTIR 5125 Tech. rep. U.S. Department of Commerce

[2] Bentz D P, Garboczi E J, Lu Y, Martys N, Sakulich A R and Weiss W J 2013 *Cement and Concrete Composites* **38** 65–74

[3] Martìn-Pèrez B, Zibara H, Hooton R D and Thomas M 2000 *Cement and Concrete Research* **30** 1215–1223

[4] Brouwers H and Florea M 2012 *Cement and Concrete Research* **42** 125–131

[5] De Weerdt K, Colombo A, Coppola L, Justnes H and Geiker M 2015 *Cement and Concrete Research* **68** 196–202

[6] Yuan Q, Shi C, De Schutter G, Audenaert K and Deng D 2009 *Construction and Building Materials* **23** 1–13

[7] Bentz D P and Garboczi E J 1991 *Cement and Concrete Research* **21** 325–344

[8] Garboczi E J and Bentz D P 1992 *Journal of Materials Science* **27** 2083–2092

[9] Zhang M, Ye G and van Breugel K 2014 *Mechanics Research Communications* **58** 64–72

[10] Ukrainczyk N and Koenders E A B 2014 *Modelling and Simulation in Materials Science and Engineering* **22** 1–24

[11] Hirao H, Yamada K, Takahashi H and Zibara H 2005 *Journal of Advanced Concrete Technology* **3** 77–84

[12] Xi Y and Bažant Z P 1999 *Journal of Materials in Civil Engineering* **11** 58–65

[13] Boddy A, Bentz E, Thomas M D a and Hooton R D 1999 *Cement and Concrete Research* **29** 827–837

[14] Li L and Page C 1998 *Computational Materials Science* **9** 303–308

[15] Samson E, Marchand J, Robert J L and Bournazel J P 1999 *International Journal for Numerical Methods in Engineering* **46** 2043–2060

[16] Marchand J 2001 *Materials and Structures* **34** 195–200

[17] Zheng J J, Zhou X Z and Wu Z M 2010 *Materials and Structures* **43** 99–106

[18] Bentz D P, Garboczi E and Lagergren E 1998 *Journal of Cement, Concrete and Aggregates* **20** 129–139

[19] Garboczi E J and Bentz D P 1998 *Advanced Cement Based Materials* **8** 77–88

[20] Zhang M, Ye G and van Breugel K 2014 *Mechanics Research Communications* **58** 53–63

[21] Nilenius F, Larsson F, Lundgren K and Runesson K 2013 *International Journal for Numerical and Analytical Methods in Geomechanics* **37** 1535–1551

[22] Nilenius F, Larsson F, Lundgren K and Runesson K 2014 *Computational Mechanics* **54** 461–472

[23] Lu Y, Garboczi E, Bentz D P and Davis J 2012 *COMSOL Conference 2012, Boston, MA, USA* 1–15

[24] Ukrainczyk N and Koenders E A B 2014 3D simulation of cement paste aging due to reactive transport *RILEM international symposium on concrete modelling (CONMOD 2014)* 1 pp 305–313

[25] Bentz D P 2005 *CEMHYD3D: A three-dimensional cement hydration and microstructure development modelling package. Version 3.0* (National Institute of Standards and Technology, U.S. Department of Commerce)

[26] Bentz D P 1997 *Journal of the American Ceramic Society* **80** 3–21

[27] Bentz D P, Mizell S, Satterfield S, Devaney J, George W, Ketcham P, Graham J, Porterfield J, Quenard D, Vallee F, Sallee H, Boller E and Baruchel J 2002 *NIST Journal of Research* **107** 137–148

[28] National Institute of Standards and Technology – NIST – US Department of Commerce, Gaithersburg, MD 2002 Visible cement dataset [online], available from: http://visiblecement.nist.gov

[29] Page C, Short N and El Tarras A 1981 *Cement and Concrete Research* **11** 395–406

[30] Ramachandran V S 1971 *Matériaux et Construction* **4** 3–12

[31] Farnam Y, Dick S, Wiese A, Davis J, Bentz D P and Weiss J 2015 *Cement and Concrete Composites* **64** 1–15

[32] Zibara H 2001 *Binding of External Chlorides By Cement Pastes* Ph.D. thesis University of Toronto - Canada

[33] Ehtesham Hussain S, Rasheeduzzafar and Al-Gahtani A S 1994 *Cement and Concrete Research* **24** 8–24

[34] Balonis M and Glasser F P 2009 *Cement and Concrete Research* **39** 733–739

[35] Bentz D P 2000 *CEMHYD3D: A three-dimensional cement hydration and microstructure development modelling package. Version 2.0* (National Institute of Standards and Technology, U.S. Department of Commerce)

[36] Taylor H F W 1997 *Cement chemistry* (London, United Kingdom: Thomas Telford Publishing)

[37] Bentz D P 2006 *Cement and Concrete Research* **36** 259–263

[38] Krabbenhoft K and Karim M R 2013 *Advances in Computed Tomography for Geomaterials: GeoX 2010* 156–163

[39] Garboczi E J and Bentz D P 2001 *Cement and Concrete Research* **31** 1501–1514

[40] Bentz D P 2006 *Journal of the American Ceramic Society* **89** 2606–2611

[41] Yu S and Page C 1991 *Cement and Concrete Research* **21** 581–588

[42] Tang L and Nilsson L O 1993 *Cement and Concrete Research* **23** 247–253

[43] Ngala V and Page C 1997 *Cement and Concrete Research* **27** 995–1007

[44] MacDonald K A and Northwood D O 1995 *Cement and Concrete Research* **25** 1407–1416